MATERIALS SCIENCE AND TECHNOLOGY
2022, VOL. 38, NO. 6, 363–376
https://doi.org/10.1080/02670836.2022.2043626

I·M3 Institute of Materials, Minerals & Mining
Taylor & Francis
Taylor & Francis Group

Recrystallisation kinetics and yield-strength adjustment after annealing of cold-rolled microalloyed steel

Pablo Bruno Paiva Leão[a], S. L. S. Medeiros[a], B. R. C. Saraiva[a], J. R. Barros Neto[b], C. C. Silva[a], Antonio J. Ramirez[c] and H. F. G. de Abreu[a]

[a]Department of Metallurgical and Materials Engineering, Universidade Federal do Ceará, Fortaleza, Brazil; [b]Department of Materials Engineering, Universidade Federal do Piaui, Teresina, Brazil; [c]Department of Materials Science and Engineering, The Ohio State University, Columbus, OH, USA

ABSTRACT

After continuous annealing process (CAP) at 790°C, 85% of the coils of 50% cold-rolled low carbon microalloyed (LCM) steel did not exhibit yield-strength (YS) on the target range, while the 70% cold-reduced LCM coils did. In this context, the non-isothermal recrystallisation kinetics of ferrite for the above two full-hard LCM steel were investigated using differential scanning calorimetry and the Friedman differential isoconversional method. The recrystallisation kinetics of ferrite for the two deformed states showed different behaviour. Regarding a fixed degree of cold-rolling deformation, the soaking temperature was found as the manageable parameter to control YS during CAP. Consequently, a suitable YS of the 50% cold-rolled LCM steel was achieved by setting the soaking temperature at 773°C.

ARTICLE HISTORY
Received 14 September 2021
Revised 31 January 2022
Accepted 2 February 2022

KEYWORDS
Low carbon microalloyed steel; method of Friedman; differential scanning calorimetry; activation energy; cold-rolling; continuous annealing process; recrystallisation; yield-strength

Introduction

Low carbon microalloyed (LCM) steels allow the use of thinner strips with suitable mechanical properties in car bodies. This achievement is a result of simultaneous improvement of strength and toughness. It is based on grain refinement during the hot-rolling process controlled by both; the solubility of precipitates in the iron matrix and the stages of the thermomechanical process [1,2]. In the subsequent cold-rolling process, dislocations are introduced into the material's crystal lattice, and consequently, work hardening occurs. Also, a non-uniform accumulation of dislocation takes place. This way, internal structures within the grains, such as subgrains, and new grain boundaries, are formed. Eventually, the grain boundary (GB) area increases and cold-deformed strips retain an amount of energy proportional to their degree of reduction. This stored energy consists essentially of the energy of all dislocations and new interfaces [3,4].

Then, the continuous annealing process (CAP) is one of the typical processing routes applied to cold-worked steel, mainly to restore its mechanical properties (softening). At CAP, cold-rolled strips of low-carbon steels are often annealed at intercritical temperatures [5]. In this circumstance, the heating rate significantly affects the metallurgical events during annealing treatment, such as ferrite recrystallisation. At a slow heating rate (< 10°C/s), ferrite recrystallisation can occur non-isothermally before austenite nucleation in cold-worked low-carbon steels, and the holding time does not affect the ferrite microstructure [6,7]. In contrast, ferrite recrystallisation is delayed by austenite transformation when the heating rate increases (> 100°C/s). Similarly, the influence of holding time and the cooling rate becomes very relevant at high heating rates [3,4,8,9].

In this context, it is known from the literature [10,11] that differential scanning calorimetry (DSC) is a powerful technique for studying phase transformations in steels and alloy materials. In addition, the DSC technique can perform non-isothermal measurements [11]. Under this circumstance, the effective activation energy (E_x) of a phase transformation fraction can be determined by isoconversional methods without assuming the kinetic-model function (model-free) [12,13]. Furthermore, several works report the application of Friedman's differential isoconversional method (FDIM) [14] in different solid-state kinetic studies: kinetic of material degradation, crystallisation and phase transformation in mould fluxes for steel casting, metallic glassy crystallisation, and phase transformation in steels and metal alloys [11,15,16]. However, studies adopting isoconversional methods for evaluating specifically recrystallisation transformation in cold-rolled steels are scarce, mainly considering different degrees of cold-deformation and correlations

CONTACT Pablo Bruno Paiva Leão pablobruno@alu.ufc.br; pbpleao@gmail.com

between the behaviour of E_x and the initial microstructure/crystallographic orientation of the material [10].

Therefore, the current work aims to describe the non-isothermal ferritic recrystallisation kinetics through DSC and model-free FDIM for the LCM steel in two distinct degrees of cold-rolled reductions (50% and 70%), to demonstrate that the model-free FDIM is a viable way to evaluate the experimental recrystallisation kinetic data. Also, electron backscatter diffraction (EBSD) analyses were used to provide crystallographic insights of both cold-worked steel conditions. Additionally, this study is based on an industrial case, in which 85% of the coils produced from the LCM steel with 50% in cold-reduction had, after CAP (at 790°C), a yield-strength (YS) value below the target range (340–420 MPa). Meanwhile, the 70% cold-rolled coils reached the suitable YS-values with the same soaking temperature. Thus, the recrystallisation kinetics results can provide technical information to solve a process issue. The results obtained from a collaboration between university and industry are reported in the following.

Materials and methods

Industrial aspects

During the hot-rolling process, the investigated LCM steel was produced with a finishing rolling temperature of 920°C (±2) and a coiling temperature of 590°C (±2). Subsequently, the strips were 50% and 70% cold-rolled reaching a final thickness of 1.6 and 0.7 mm, respectively. In addition, industrial data from CAP were evaluated to establish relationships among strip thickness, strip speed, soaking temperature and YS.

50% and 70% cold-rolled samples

Full-hard steel samples were collected from the central position of both 50% and 70% cold-rolled strips at the entrance of CAP, and their crystallographic textures and kinetics were evaluated in this work. The chemical composition of both full-hard steel conditions obtained by optical emission spectrometer (THERMO-ARL 4460 M) is shown in Table 1. The samples were prepared through the regular metallographic procedure based on grinding and polishing, using sandpapers (from #100 to #2000 grit) and diamond suspension (6, 3, and 1 µm). At that point, the samples were etched in 2% Nital solution for microstructural observations performed in an optical microscope (ZEISS model Axio Imager 2). For microtexture investigation, the sample preparation procedure received a final vibratory polishing step with 0.04 µm colloidal silica for one hour. The EBSD maps were acquired employing a scanning electron microscope (model Quanta 450 FEG-FEI) coupled with an EBSD detector (Oxford Instruments, Oxford, UK). The EBSD analysis was carried out using an operating voltage of 20 kV, a step size of 100 nm, a working distance of 10 mm and a sample tilt angle of 70°.

Regarding recrystallisation kinetics, four rectangular samples, for each aforesaid full-hard strip, were ground (using sandpaper of #200 grit) up to dimensions of 2 (width) × 4 (length) × 0.5 (thickness) mm³ for removing oxide contamination. Then, the rectangular ground samples were immediately used in the DSC technique through a NETZSCH machine (model TG-DSC STA 449 F3 Jupiter). This analysis was executed at four constant heating rates (10, 15, 25 and 30°C/min) from room temperature up to 720°C in the argon gas atmosphere. The Friedman method [14] was used to calculate the effective activation energy from the DSC thermograms.

50% cold-rolled samples after CAP

For adjusting YS after CAP of the 50% cold-rolled strip, twenty-three tensile samples were collected on the central position of the galvanised strip for each assessed soaking temperature (760°C, 780°C, 790°C, 805°C and 830°C). Meanwhile, the other parameters were kept as consistent as possible (heating rate around 10°C/s, cooling rate around 15°C/s, strip's speed around 60–80 m/min, soaking time about 50 s, strip's thickness of 1.6 mm, and skin pass mill of 1.2%). In this context, planar and normal anisotropy properties were also measured for the annealed strips in each investigated soaking temperature from the following equations:

$$\text{Normal Anisotropy,} \quad \bar{r} = (r_0 + 2r_{45} + r_{90})/4 \tag{1}$$

$$\text{Planar Anisotropy,} \quad \Delta r = (r_0 - 2r_{45} + r_{90})/2 \tag{2}$$

The anisotropy parameters (r_0, r_{45}, r_{90}) were obtained in duplicate from tensile tests. In this case, the tensile samples were orientated in 0°, 45° and 90°, concerning the strip's rolling direction. The NBR ISSO 6892-1standard was employed for the tensile test performance and tensile specimen dimensions. These tests were performed using an Instron 5582–100KN Universal Testing Machine. Furthermore, the average grain

Table 1. Compositions of the cold-rolled LCM steel samples (wt%).

Sample	C	Mn	P	S	Si	Ni	Cr	Al	Ti	Nb	N	Fe
50% cold-rolled steel	0.049	0.548	0.018	0.007	0.005	0.005	0.012	0.056	0.03	0.001	0.0043	Bal.
70% cold-rolled steel	0.048	0.514	0.016	0.008	0.007	0.006	0.015	0.062	0.03	0.001	0.0041	Bal.

size was determined according to the ASTM E112 standard.

Regarding the influence of the holding time and soaking temperature on the amount of austenite formed during CAP, the commercial software JMatPro® [17] was employed. The model of JMatPro® for simulating the reaustenitisation of steels is based on the modified Johnson-Mehl-Avrami equation [18]. The thermodynamic calculation was performed using, as input data, the chemical composition of the 50% cold-rolled steel in Table 1, the heating rate of 10°C/s, and the microstructural condition set as normalised. Moreover, different holding times (50 and 70 s) and soaking temperatures (760°C, 780°C, 790°C, 805°C and 830°C) were inserted for doing many calculations. In this case, the software assumes an initial microstructure of a mixture of ferrite and pearlite/carbides, and that the kinetics of reaustenitisation are limited by carbon diffusion. During heating, it is also adopted that, regions with carbides first transform into austenite, followed by ferrite. Finally, the starting transformed austenite is inhomogeneous, and the further austenite homogenisation is a function of the holding time and soaking temperature of reaustenitisation.

Results and discussion

Microstructure and microtexture of the steel in the cold-rolled states

Figure 1(a, b) shows the optical micrographs on the cross-section region of the LCM steel strips in the 50% and 70% cold-rolled conditions. Notably, the ferritic grains are flattened in a pancake-like shape. The 70% cold-worked strip presents smaller grains (an average thickness of 1.74 μm) than in the 50% deformed state (an average thickness of 3.33 μm). Also, cementite particles were found more spread out on the ferritic matrix and smaller in the 70% deformed one. The average lengths of the cementite particles were 6.77 and 2.59 μm, respectively, for 50% and 70% cold-worked steel.

The colour-coded inverse pole figure (IPF) maps in Figure 2(a, b) show the subsurface microstructures of the full-hard samples in the abovementioned cold-rolled conditions. In both cases, it is possible to realise that the ferritic grains are stretched along the rolling direction (RD), bound by GB or high angle grain boundaries (defined by $\theta \geq 15°$ and shown by black lines). Inside the ferritic grains, there is a high density of subgrain boundaries or low angle grain boundaries (defined by $2° \leq \theta < 15°$ and shown by white lines) where, on the analysed area, they represented a fraction of 78% and 83%, respectively, for the 50% and 70% cold-deformed states. The black points in Figure 2(a, b) were regions that could not reach suitable Kikuchi patterns.

Furthermore, the orientation distribution function (ODF) from the individual IPF maps is shown in Figure 3(a, b), and their intensities are expressed in multiple random densities (mrd). In both cases, the ODFs displayed similar fibres, a partial α-fibre and a γ-fibre, but with distinct component intensities. Specifically, the 50% cold-rolled strip revealed a dominant *α-fibre*, in which $113 \approx 112 < 110 >$ was the component in sharper intensity (6.7 mrd). This outcome may be attributable to prior deformed austenite during the hot-rolling process [19]. Conversely, the 70% cold-rolled strip exhibited a dominance of γ-fibre with $111 < 112 >$ as the strongest orientation (8.2 mrd), which can be developed during cold-rolling reduction [20].

Moreover, from different techniques, it is well established that the stored energy in *γ-fibre* orientations is higher than in α-fibre orientations [21,22]. Particularly, it has been pointed out that, along the *γ-fibre*, the $111 < 112 >$ component presents the higher stored energy [23]. So, the 70% cold-rolled steel gives metallurgical features that indicate a state of higher stored energy than in the 50% cold-rolled one.

The activation energy (E_x) of ferrite recrystallisation

Figure 4 shows the DSC thermograms for the studied LCM steel at different heating rates. Each thermogram showed two exothermic events, which were confirmed by the first derivative of the DSC curve. The exothermic peaks, whose onset and final temperatures are outlined by continuous lines, are in a temperature range corresponding to ferrite recrystallisation of cold-rolled steel with similar characteristics to the steel under study [10,24,25]. The smooth peaks pointed by arrows in Figure 4 were considered recovery events. Moreover, the recovery and recrystallisation phenomena must be visible as exothermic peaks during heating due to the release of stored energy accumulated during the cold-rolling process [26]. In this regard, the kinetic evaluations will focus on the recrystallisation peaks, in which the dashed lines represent their peak temperatures.

The recrystallisation fraction (x) from the DSC thermograms as a function of temperature was reached by evaluating the partial area above the recrystallisation peaks by using Equation 3, which must result in sigmoidal curves for each heating rate

$$x(T) = A_T/A \tag{3}$$

where A_T is the partial area between the onset and a chosen transformation temperature and A is the total area from the onset up to the final transformation temperature of the exothermic peak. The recrystallisation fraction (x), as a function of the time, can be obtained by using the following equation:

$$t = (T - T_0)/B \tag{4}$$

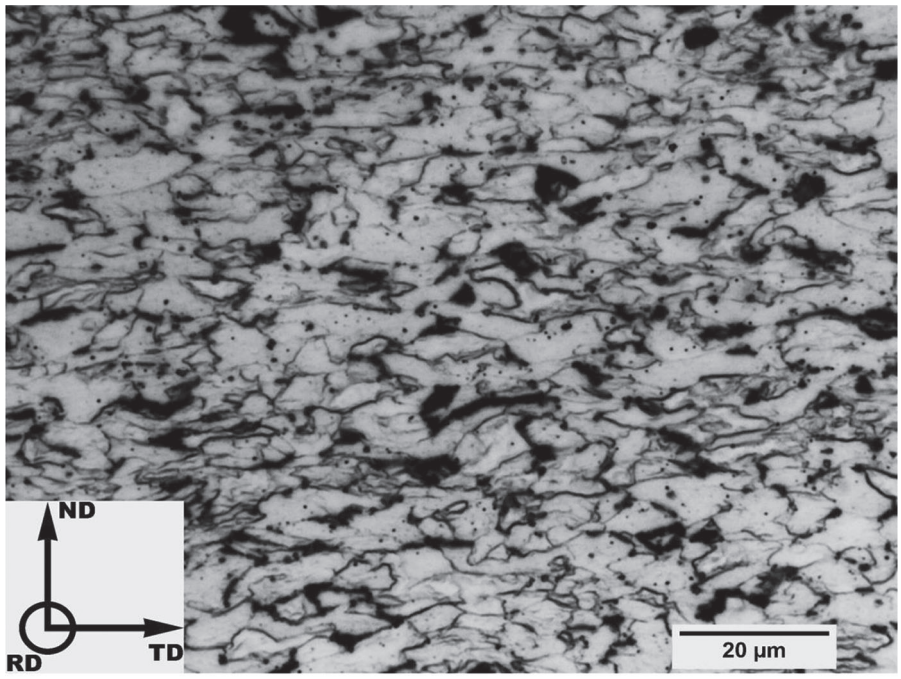

(a)

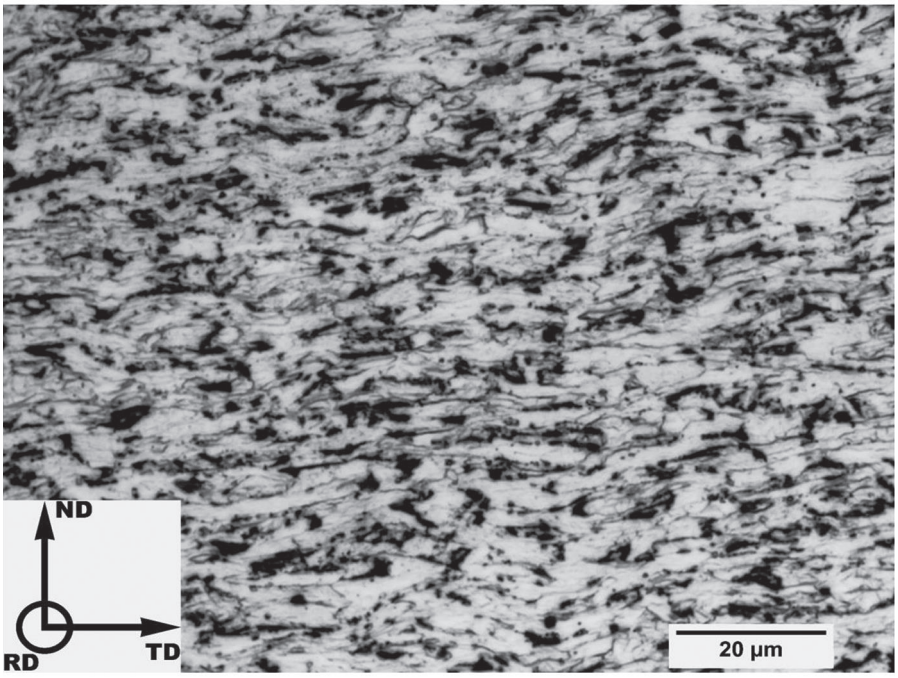

(b)

Figure 1. Optical microstructure (1000× of magnification) on the cross-section of (a) 50% cold-rolled LCM steel and (b) 70% cold-rolled LCM steel.

where B is the heating rate, T_0 is the temperature at the beginning of the transformation ($t = 0$) and T is the temperature at a given time t during the recrystallisation process. Figure 5 depicts the degree of recrystallisation as a function of time. After that, it is possible to calculate the instantaneous recrystallisation rate dx/dt through the derivation of the curves in Figure 5, and then, it can be plotted the ln(dx/dt) against x. This information will be used to calculate the ferrite recrystallisation kinetics. In this context, the effective activation energy was estimated by using the FDIM [14] through the following equation:

$$\ln (dx/dt)_x = -E_x/(RT_x) + C \tag{5}$$

where C is a constant, R is the gas constant, E_x, $(dx/dt)_x$ and T_x are, respectively, the effective activation energy, the instantaneous recrystallisation rate and the temperature at a relative x. So, the data ln(dx/dt) and T can be collected for the same x through the prior described plots x versus T and ln(dx/dt) versus x. Then,

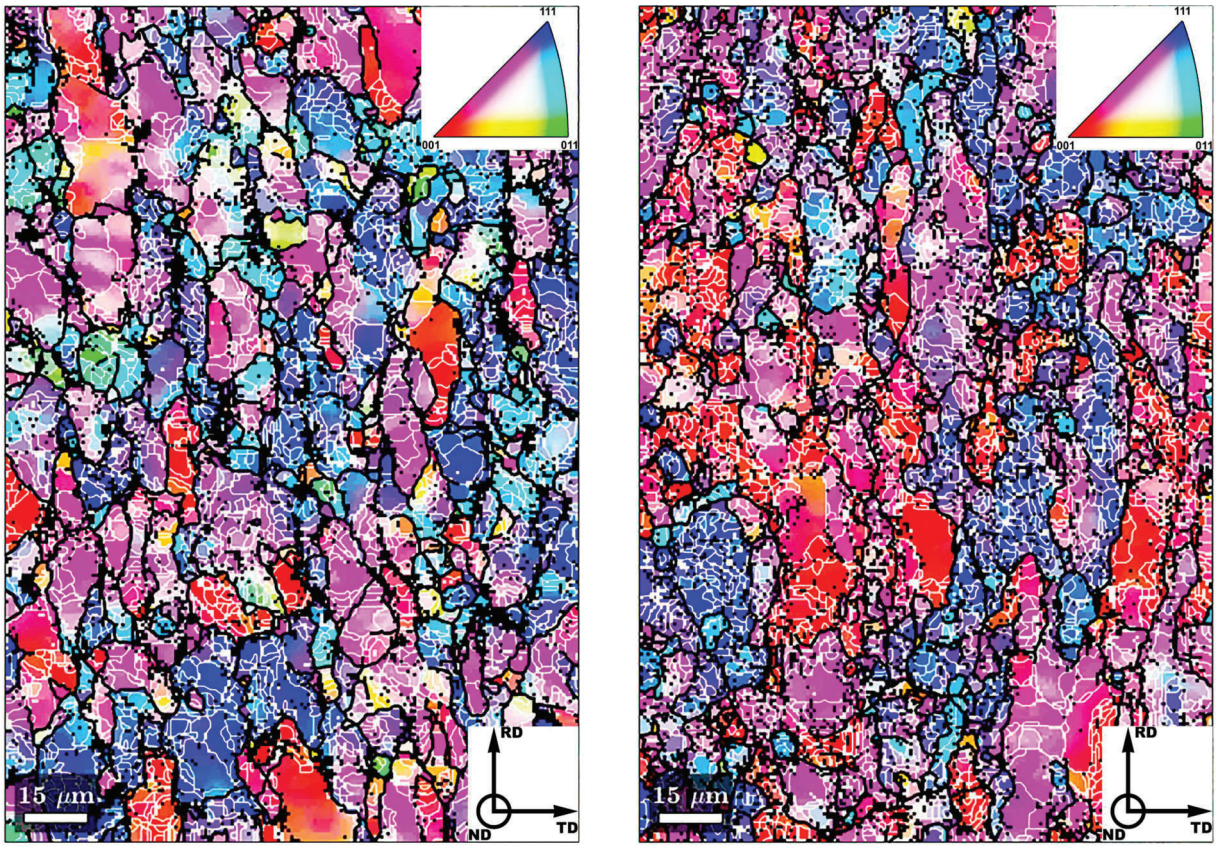

Figure 2. Colour-coded inverse pole figure (IPF) map on the subsurface region (below $\frac{1}{4}$ of the initial thickness) of (a) 50% cold-rolled LCM steel and (b) 70% cold-rolled LCM steel.

by plotting $ln(dx/dt)$ against $1000/T_x$ for each x of the four assessed heating rates, it must give a straight line with a slope (E_x/R), as presented in Figure 6. Finally, based on Equation 5, the activation energy can be estimated.

Figure 7 shows the dependence of the effective activation energy on the recrystallised ferritic fraction of the investigated LCM steel in both evaluated degrees of deformation. It can be seen that the change in the dependence of E_x is not similar between the two conditions. The 50% cold-rolled steel displays an almost unchanged performance over the x from 0.2 to 0.4. This regime is related to the fact that it is mainly governed by the nucleation step [27]. In contrast, the more deformed conditions did not exhibit this constant regime, suggesting that it may have a faster nucleation rate during heating. This evidence is consistent with the metallurgical features found in the full-hard coils, in which the nucleation rate of new grains depends on the initial state of stored energy [3].

Regarding the regimes in which the E_x increases in Figure 7, these stages may involve simultaneous nucleation and crystal growth mechanisms [27]. However, after the initial nucleation, recrystallisation may be dominated mainly by the consumption of the deformed grains by the growth of the new recrystallised grains. In this context, the 70% cold-rolled steel exhibited a lower rate of increase of E_x, concerning the same regime in the less deformed state ($x \geq 0.6$). This indicates that recrystallised grain growth is slower in the 70% cold-rolled material than in the less deformed steel [3]. In this way, the 70% cold-rolled steel has some aspects that can explain its slowed grain growth kinetics. One of them is the smaller and more widely distributed cementite particles. They may pin the recrystallised grains and thus prevent their coarsening [28]. Another is the $111 < 112 >$ deformed grains with higher stored energy, in which the number of nuclei formed should be larger, and the proportion of recrystallised grains should initially increase more rapidly. This event may lead to the meeting of the new free-dislocation grain boundaries, still in small sizes. Consequently, the recrystallisation rate will tend to decrease due to pinning between the new GBs [3].

Additionally, recent studies [29,30] reported that in multi-phase steels with ductile matrix and hard second phase particles, the GB's and matrix/second phase particles interfaces are prone to accumulation of strain/dislocation during plastic deformation. Based on this, it may be considered that smaller grain size (larger number of GB per unit area) and less agglomerated cementite particles (more ferrite/cementite interfaces)

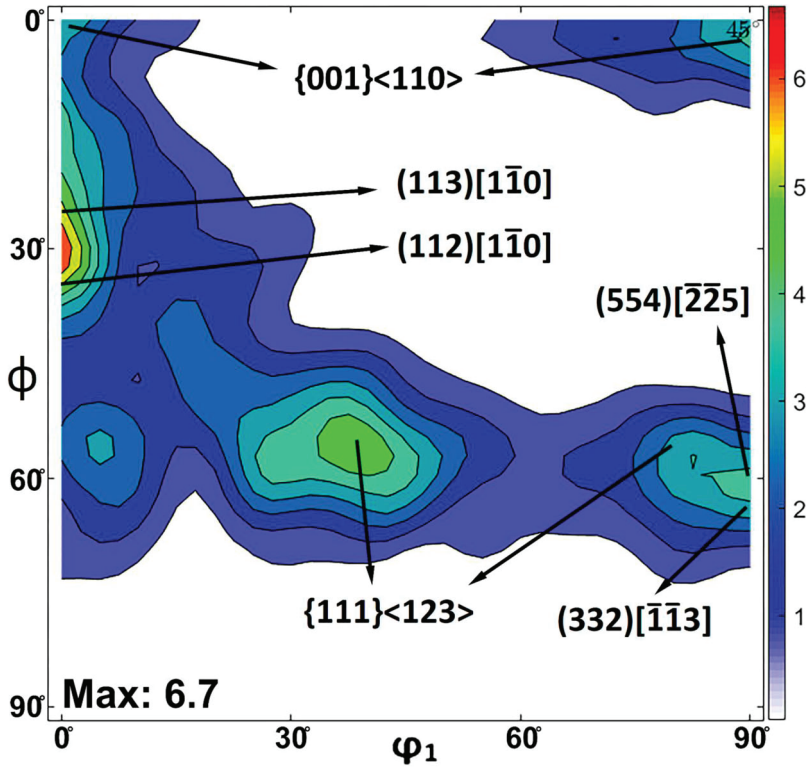

(a)

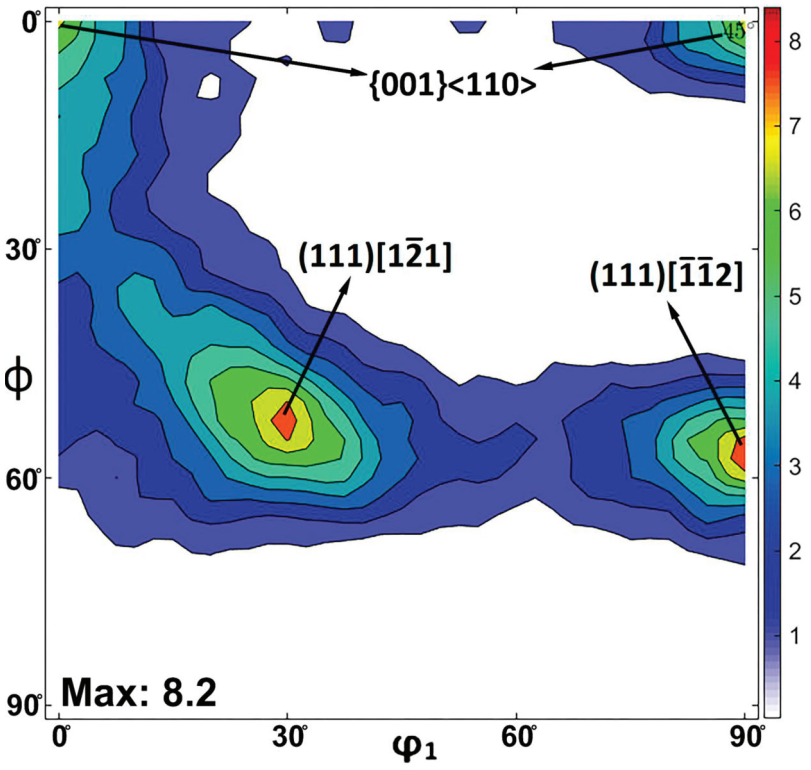

(b)

Figure 3. Orientation distribution function (ODF) at $\varphi_2 = 45^\circ$ of (a) 50% cold-rolled LCM steel and (b) 70% cold-rolled LCM steel.

in the 70% cold-rolled steel can also contribute to increasing the start number of sites during the recrystallisation process. Moreover, it is known from the literature [31] that carbonitride particles may also significantly influence pinning grain growth in Ti/Nb stabilised steels. These precipitates' characteristics and pinning effect are primarily determined by the hot-rolling and coiling parameters, identical in the

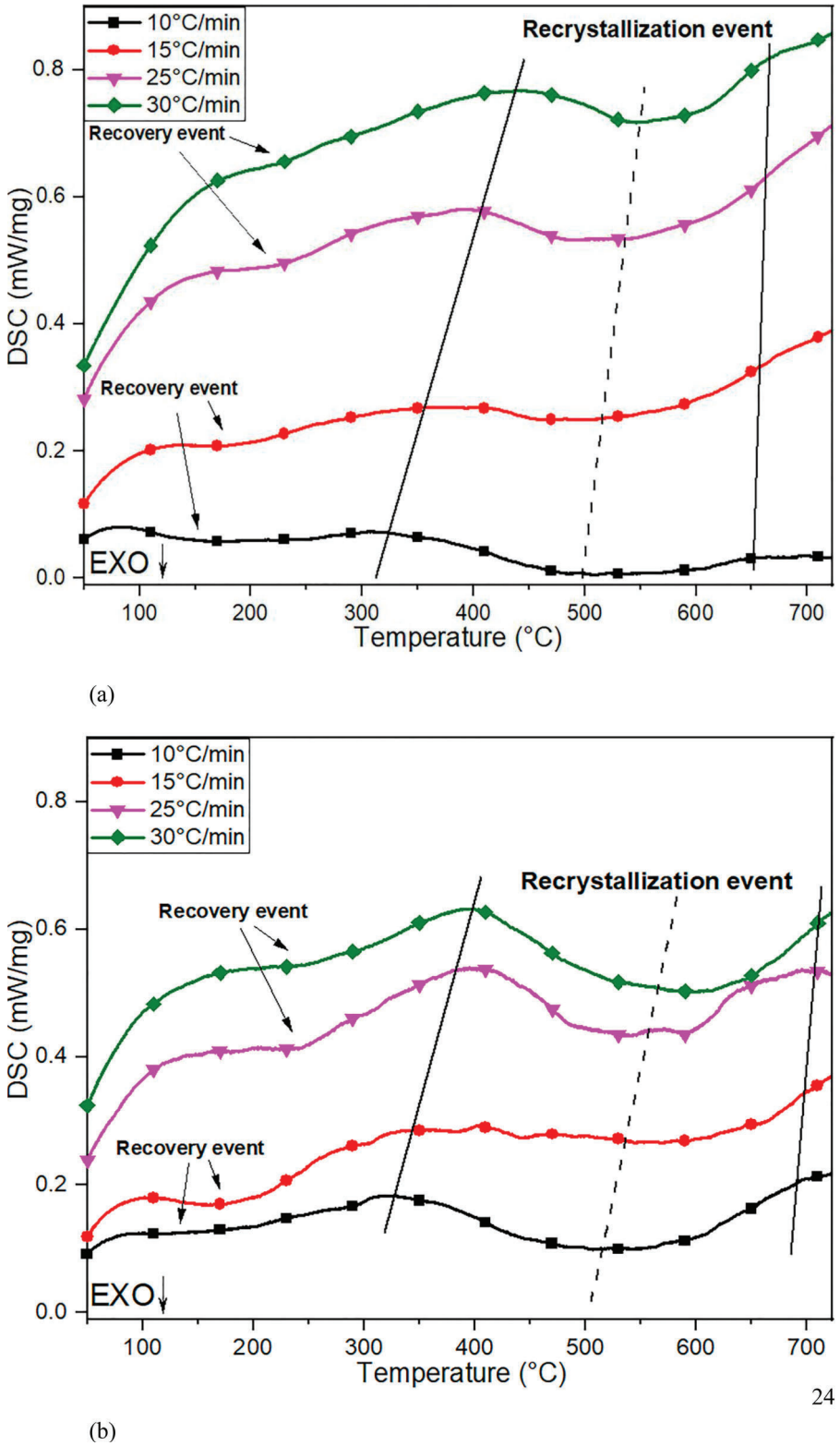

Figure 4. DSC thermograms at different heating rates (10, 15, 25 and 30°C/min) of (a) 50% cold-rolled LCM steel and (b) 70% cold-rolled LCM steel.

evaluated conditions. Therefore, this pinning effect was considered equivalent in both cases.

CAP industrial data

Figure 8(a) displays a relationship between strip thickness and its respective average production speed. The latter represents the average velocity that the strip runs in the CAP line. During CAP, the strip thickness variation can be considered an independent variable because it results from a previous process parameter (degree of reduction during the cold-rolling process). As observed in Figure 8(a), average strip speed has an inversely proportional dependence on the strip thickness. This behaviour is mainly related to strip thickness and its weight, impacting the plant's security and operational

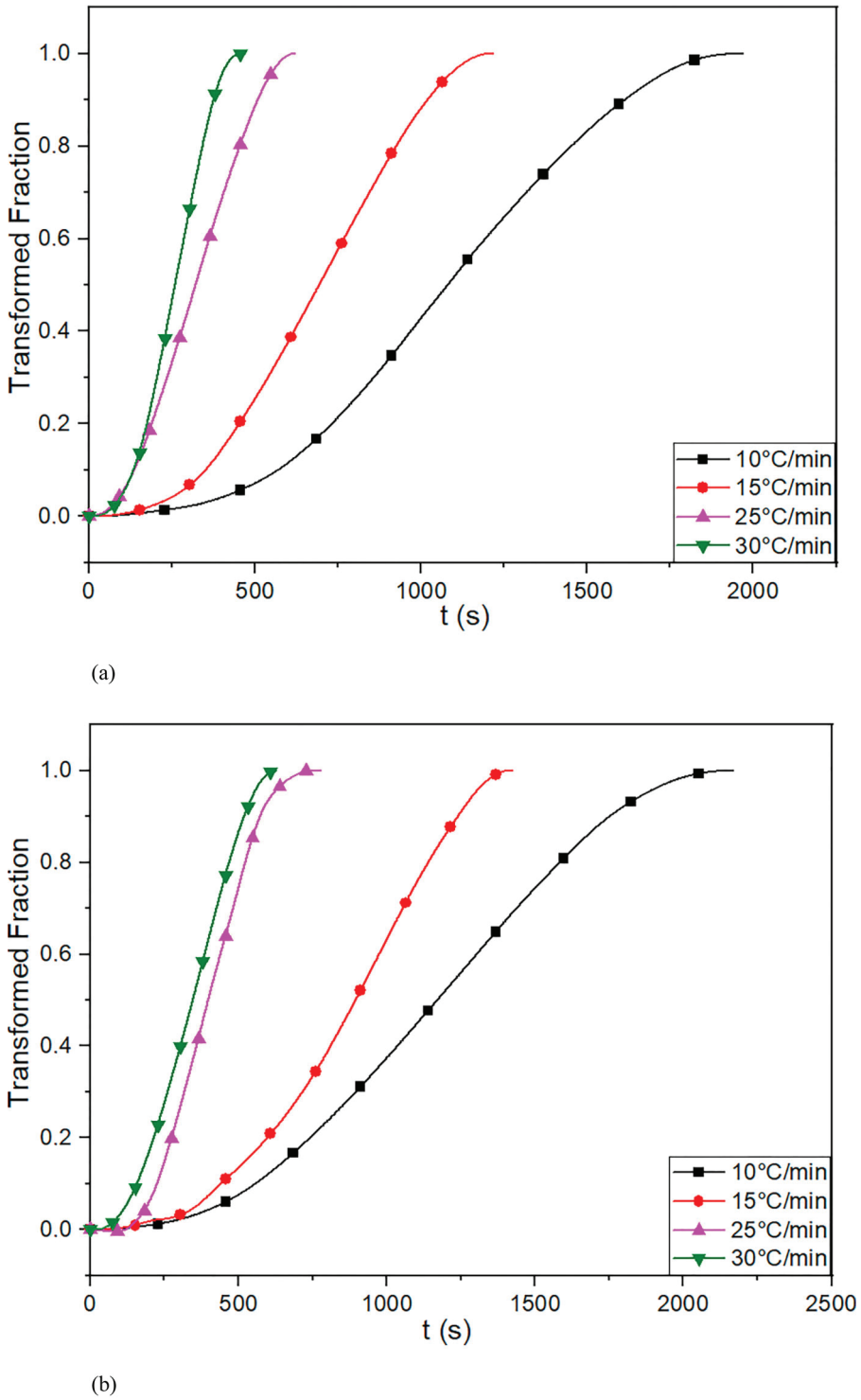

Figure 5. Recrystallisation fraction (x) of full-hard LCM steel as a function of time (s), at different heating rates (10, 15, 25 and 30°C/min) for (a) 50% cold-rolled LCM steel and (b) 70% cold-rolled LCM steel.

capacity. Moreover, it could present a significant speed variation during CAP along with the same coil. So, the strip's speed is not entirely manageable because it depends on the coil's thickness and the process stability.

Furthermore, Figure 8(b) exhibits the strip speed versus soaking temperature of CAP and both as a function of YS (in contour plot colour). For the evaluation of Figure 8(b), it is essential to take into account the relationship described in Figure 8(a). In particular, Figure 8(b) shows YS divergence at a constant soaking temperature and different strip speeds. In this case, two significant factors, with simultaneous effects, can be recognised; the holding time and previously discussed ferritic recrystallisation kinetics. To summarise, thinner strips (higher cold-reduction) with disadvantageous kinetics for ferritic grain growth are mainly

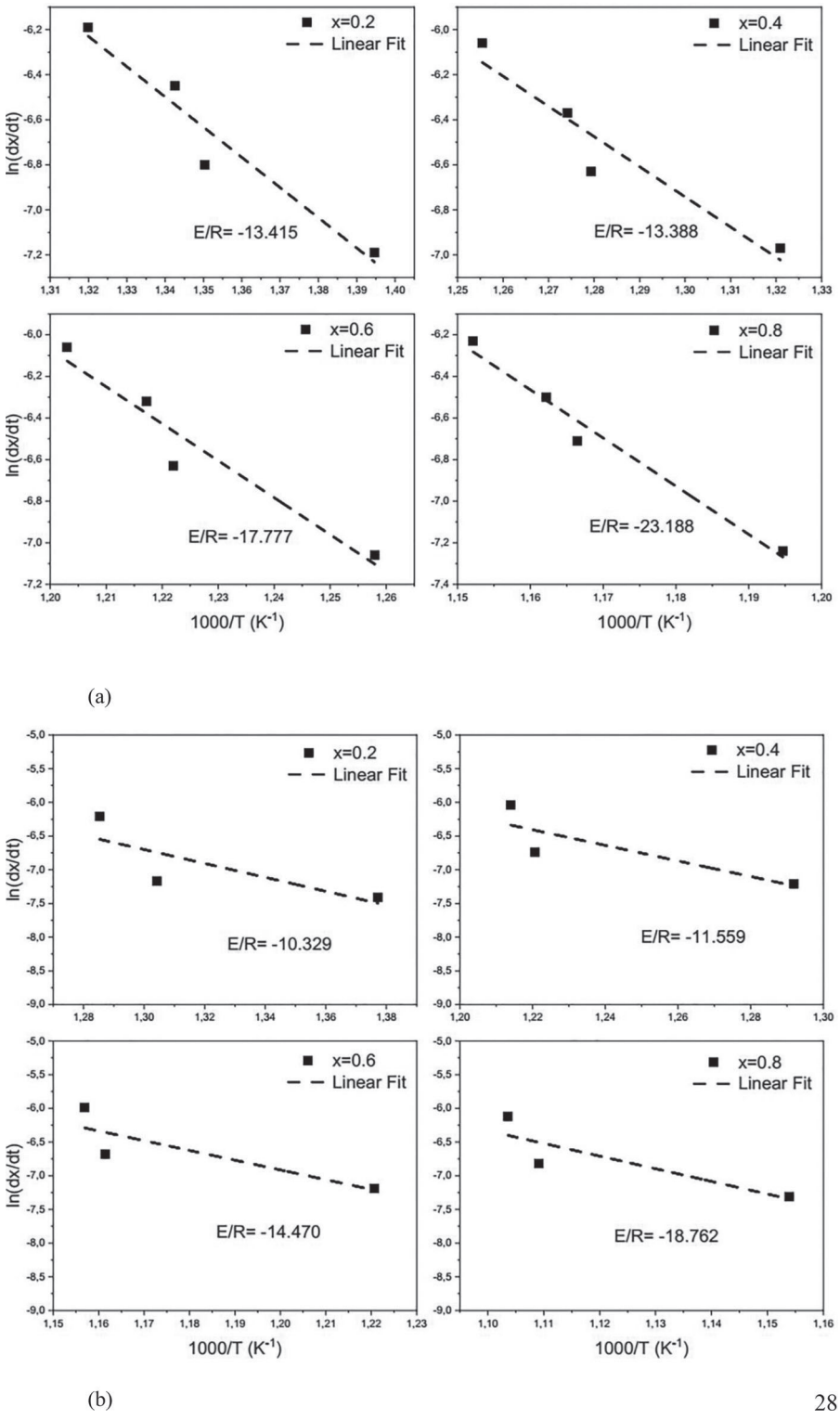

28

Figure 6. ln(dx/dt) as a function of $1000/T_x$ for different recrystallisation fraction of LCM steel for (a) 50% cold-rolled LCM steel and (b) 70% cold-rolled LCM steel.

produced in higher velocities (shorter holding time), remaining in the higher range of YS. While, thicker strips (lower cold-reduction) with favourable kinetics for ferritic grain growth are manufactured in lower velocities (longer holding time), staying in the lower range of YS. In this way, considering the Hall-Petch [32] relationship, the thicker strips may have a larger final ferritic grain size after CAP than the thinner ones.

Also, the austenite phase is formed at intercritical temperatures and is converted into ferrite during cooling [5,6,7]. It is well known that austenite mainly nucleates in ferritic GBs and ferrite/Fe_3C interfaces, and the diffusion phenomenon controls its growth [5,6,7,33]. Therefore, it suggests that at the intercritical temperature during the annealing, austenite may nucleate in several sites with a shorter time for growing in the

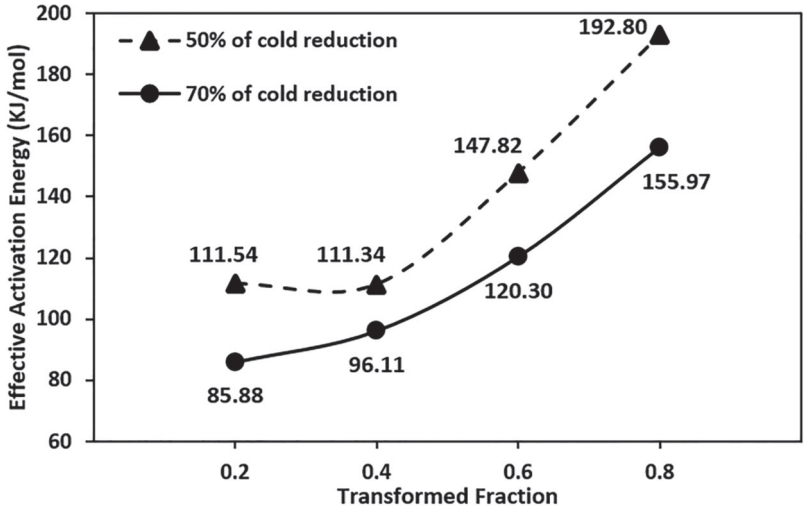

Figure 7. Effective activation energy for recrystallisation (E_x) of LCM steel as a function of recrystallised fraction for the investigated cold-rolled conditions.

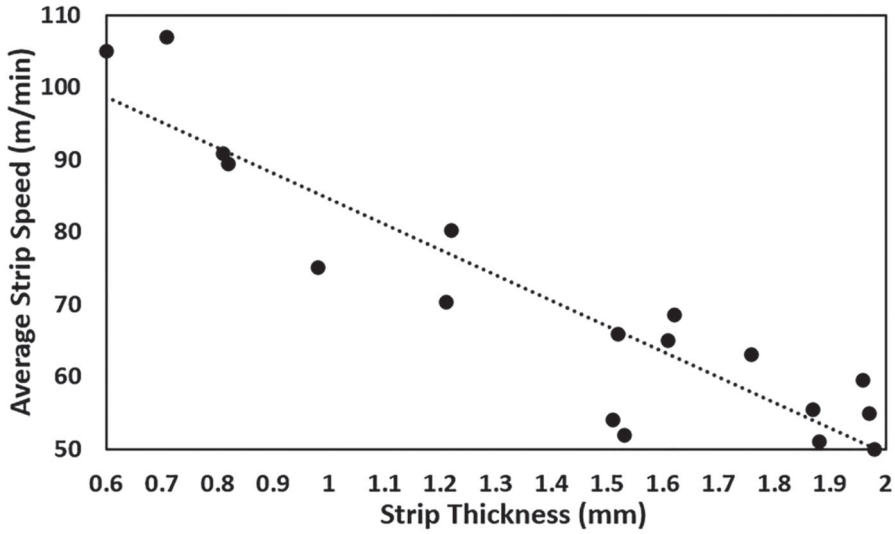

(a)

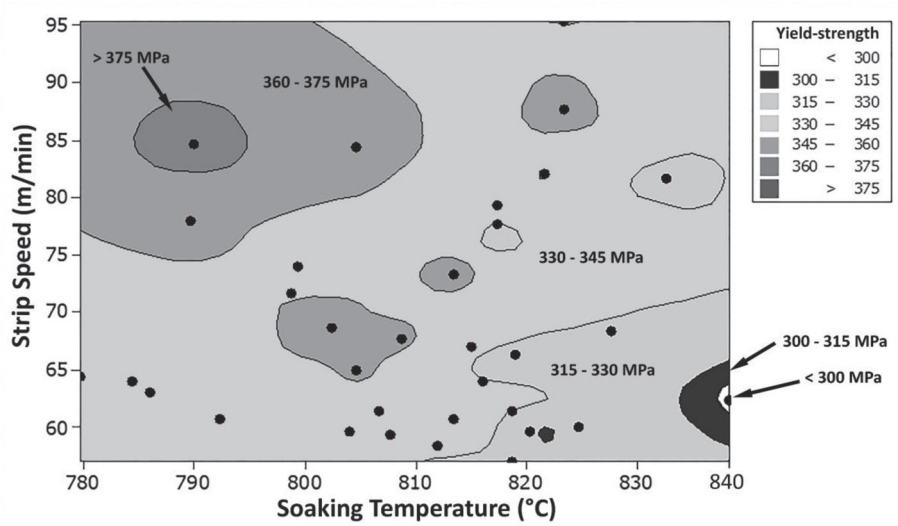

(b)

Figure 8. Correlation of parameter data from continuous annealing process: (a) average strip speed as a function of strip thickness and (b) strip speed and soaking temperature as a function of yield strength.

thinner strips. In contrast, it has fewer sites for nucleating and a longer time for growing in the thicker strips. Thus, these strips may have different final ferritic grains, even after CAP at the same soaking temperature, resulting in the YS variation, as in the 50% and 70% cold-rolled steels investigated in this work.

Furthermore, it is also possible to observe in Figure 8(b) a strong effect on YS by varying the soaking

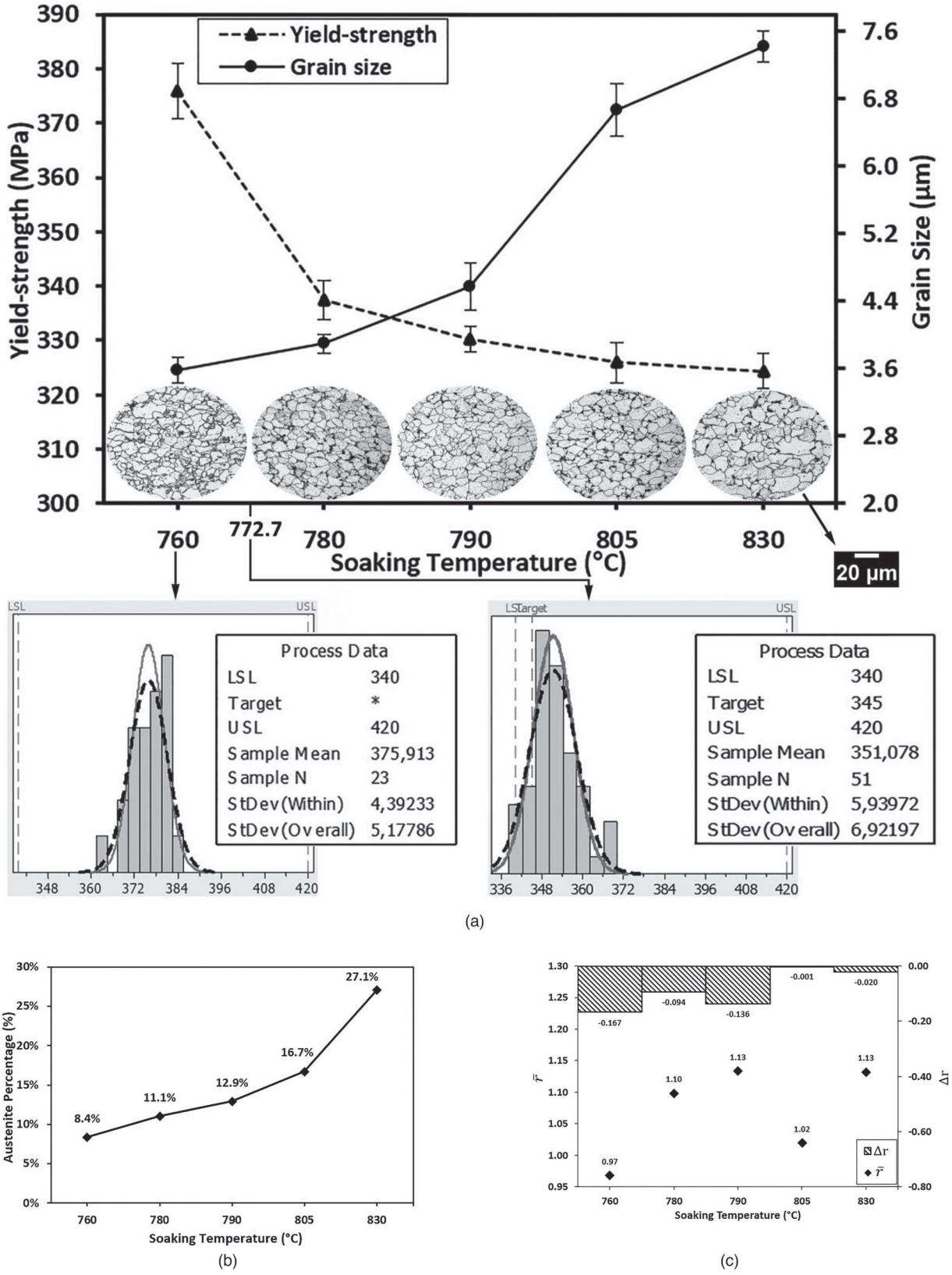

Figure 9. (a) Yield strength and ferritic grain size, (b) JMatPro® simulation of austenite formation at holding times of 50 and 70 s and (c) anisotropic properties (planar and normal) for the 50% cold-rolled strip as a function of soaking temperature.

temperature at a determined speed. It means almost constant thickness or slight divergence in the degree of cold-rolling deformation. Therefore, considering the YS adjustment for a fixed thickness and the link between the strip speed and its respective thickness, it is evident that the soaking temperature is the controllable parameter during CAP to control YS.

YS adjustment and anisotropy properties for the 50% cold-rolled LCM steel

Considering only the 50% cold-rolled LCM steel, Figure 9 shows the effect of the soaking temperature of CAP on its YS, ferritic grain size, percentage simulated of austenite formed during intercritical temperature and anisotropy properties. It can be seen in Figure 9(a) that the grain size and YS are inversely proportional, which is consistent with the Hall-Petch relationship [32]. Also, no deformed ferrite grains were found in the 50% cold-rolled LCM steel microstructures after CAP. In contrast, it consisted of equiaxed ferrite grains with some spheroidised cementite in their grain boundaries. It suggests that the complete ferrite recrystallisation occurred before austenite formation [6,33]. Furthermore, the normal distributions in Figure 9(a) depict that the central position (average of 375.93 MPa) of the YS aimed range (340–420 MPa) was achieved by using an annealing temperature of 760°C. However, to minimise efforts in the dye during the subsequent stamping process, it is essential to target the YS in the lower limit. So, an average YS of 351.07 MPa, close to the YS minimum limit, was obtained for 51 coils with an average soaking temperature of 772.7°C.

In addition, simulation of phase transformation using JMatPro® software revealed a strong dependence of the soaking temperature on the amount of austenite formed during intercritical annealing, as shown in Figure 9(b). This temperature dependence may be explained by the diffusion phenomenon that controls the growth of austenite nuclei [6,7,33]. This suggests that the final ferritic grain size is mainly influenced by the amount of austenite formed during intercritical annealing. Furthermore, the variation in holding time during the manufacture of the 50% cold-worked LCM steel in CAP is short (about 50–70 s), and the amount of austenite shown in Figure 9(b) was the same in the range of 50–70 s.

After CAP, the investigated steel is shaped into safety parts of car bodies (such as centre pillar reinforcement and inner lock pillar) via the conventional/deep drawing process. In this setting, the anisotropy properties of the 50% cold-worked LCM steel, after CAP, are presented in Figure 9(c). These properties did not show a noticeable variation between the investigated soaking temperatures. The planar anisotropy (Δr) values ranged from 0.166 to −0.001, which are near zero, meaning that the material has a low tendency for earing during the drawing process. For normal anisotropy ($\bar{r}$), which represents the resistance of the strip for thinning during plastic deformation, the $\bar{r}$-values ranged from 0.97 to 1.13. It is worth realising that the smaller $\bar{r}$-value found is close to 1, which is a reference for isotropic flow strengths in the strip. Therefore, it is reasonable to consider that the formability properties of the 50% cold-rolled steel, after CAP, are employable for the conventional drawing process [34,35].

Conclusions

In this work, an industrial case study was considered. After a similar continuous annealing process (CAP) at 790°C, the 50% and 70% cold-rolled LCM steel presented, respectively, YS below and YS on the aimed target (340-420 MPa). Therefore, ferritic recrystallisation kinetics of the 50% and 70% cold-rolled LCM steel were investigated via DSC and model-free FDIM. Subsequently, CAP parameter data were evaluated. Finally, grain size, YS, normal, and planar anisotropy were measured after CAP for the 50% cold-rolled LCM steel. The conclusions are as follows:

(1) The model-free FDIM proved to be a feasible way to predict the ferritic recrystallisation kinetics from experimental DSC data regarding different degrees of cold-rolled deformation of LMC steel.
(2) The ferritic recrystallisation kinetics profiles determined via model-free FDIM showed different behaviour for the two cold-rolling conditions studied. The less deformed steel exhibited slower nucleation and faster grain growth rate, resulting in a trend towards a larger recrystallised ferrite final grain size. In contrast, the higher cold-deformed material exhibited the opposite behaviour. This comportment could be explained by both deformed states' initial microstructure and crystallographic orientation.
(3) The evaluated CAP parameters showed a linear correlation between the speed and the thickness of the strips due to their weight. The intercritical soaking temperature was the dominant parameter under YS for a given thickness.
(4) The arrangement between the information from ferrite recrystallisation kinetics and the CAP parameter assessments contributed to understanding the YS divergence of manufactured strips in different thicknesses and at a given soaking temperature.
(5) The appropriate YS for the 50% cold-rolled continuously annealed steel was achieved by adjusting the soaking temperature, which significantly affected the ferritic final grain size. Otherwise, the anisotropy properties showed no significant difference with the variation of soaking temperature.

Acknowledgments

The authors acknowledge the following facilities of Universidade Federal do Ceará; Laboratório de Caracterização de Materiais (LACAM), Laboratório de Fundição (LaF), and Central Analítica UFC/CT-INFRA FINEP/Pro-Equipamentos-CAPES/CNPq-SisNano-MCTI 2019 (Grant 442577/ 2019-2)-INCT-FUNCAP for providing support in this work.

Disclosure statement

No potential conflict of interest was reported by the author(s).

Funding

This study was financed in part by the Coordenação de Aperfeiçoamento de Pessoal de Nível Superior – Brasil (CAPES) – Finance Code 001.

References

[1] Lesch C, Klose FB. Advanced high strength steels (AHSS) for automotive applications – tailored properties by smart microstructural adjustments. Steel Res Int. 2017;38:1–21. DOI: 10.1002/srin.201700210.

[2] Baker TN. Titanium microalloyed steels. Ironmak Steelmak. 2019;46:1–55. DOI: 10.1080/03019233.2018.1446496.

[3] Humphreys J, Rohrer SG, Rollett A. Recrystallization and related annealing phenomena recrystallization and related annealing phenomena. Amsterdam: Elsevier; 2017.

[4] Martínez-de-Guerenu A, Jorge-Badiola D, Gutiérrez I. Assessing the recovery and recrystallization kinetics of cold rolled microalloyed steel through coercive field measurements. Mater Sci Eng A. 2017;691:42–50. DOI: 10.1016/j.msea.2017.03.033.

[5] Toji Y, Yamashita T, Nakajima K, et al. Effect of Mn partioning during intercritical annealing on following $\gamma \rightarrow \alpha$ transformation and resultant mechanical properties of cold-rolled dual phase steels. ISIJ Int. 2011;51:818–825. DOI: 10.2355/isijinternational.51.818.

[6] Chbihi A, Barbier D, Germain L, et al. Interactions between ferrite recrystallization and austenite formation in high-strength steels. J Mater Sci. 2014;49:3608–3621. DOI: 10.1007/s10853-014-8029-2.

[7] Valdes-Tabernero MA, Celada-Casero C, Sabirov I, et al. The effect of heating rate and soaking time on microstructure of an advanced high strenght steel. Mater Caract. 2019;155:109822. DOI: 10.1016/j.matchar.2019.109822.

[8] Muljono D, Ferry M, Dunne DP. Influence oh heating rate on anisothermal recrystallization in low and ultra-low carbon steels. Mater Sci Eng A. 2001;303:90–99. DOI: 10.1016/S0921-5093(00)01882-7.

[9] Ferry M, Muljono D, Dunne DP. Recrystallization kinetics of low and ultra low carbon steels during high-rate annealing. ISIJ Int. 2001;41:1053–1060. DOI: 10.2355/isijinternational.41.1053.

[10] Torres RCE, Sánchez FH, González A, et al. Study of the kinetics of the recrystallization of cold rolled low-carbon steel. Metall Mater Trans A. 2002;33A:25–31. DOI: 10.1007/s11661-002-0003-y.

[11] Shu Q, Klug JL, Medeiros SLS, et al. Crystallization control for fluorine-free mold fluxes: effect of Na_2O content on non-isothermal melt crystallization kinetics. ISIJ Int. 2020;60:2425–2435. DOI: 10.2355/isijinternational.ISIJINT-2020-132.

[12] Simon P. Isoconversional methods. J Therm Anal Calorim. 2004;76:123–132. DOI: 10.1023/B:JTAN.0000027811.80036.6c.

[13] Criado JM, Sánchez-Jiménez PE, Pérez-Maqueda LA. Critical study of the isoconversional methods of kinetic analysis. J Therm Anal Calorim. 2008;92:199–203. DOI: 10.1007/s10973-007-8763-7.

[14] Friedman HL. Kinetics of thermal degradation of char-forming plastics from thermogravimetry. Application to a phenolic plastic. J Polym Sci C. 1964;6:183–195. DOI: 10.1002/polc.5070060121.

[15] Lad KN, Savalia RT, Pratap A, et al. Isokinetic and isoconversional study of crystallization kinetics of a Zr-based metallic glass. Thermochim Acta. 2008;473:74–80. DOI:10.1016/j.tca.2008.04.011.

[16] Liu Q, Qian D, Hua L. Transformation from non-isothermal to isothermal tempering of steel based on isoconversional method. J Mater Sci. 2018;53:2774–2784. DOI: 10.1007/s10853-017-1680-7.

[17] Sente Software Ltd. (2021). JMatPro® [Internet] Guildford: Surrey Research Park [cited 2021 Dec 8]. Available from: https://www.sentesoftware.co.uk/.

[18] Bourezg YI, Elfiad D, Azzeddine H, et al. Investigation of recrystallization kinetics in hot-rolled Mg-La alloy using differential scanning calorimetry technique. Thermochim Acta. 2020;690. DOI: 10.1016/j.tca.2020.178688.

[19] Ray RK, Jonas JJ, Guillén MP, et al. Transformation textures in steels. ISIJ Int. 1994;34:927–942. DOI: 10.2355/isijinternational.34.927.

[20] Tóth LS, Jonas JJ, Daniel D, et al. Development of ferrite rolling textures in low- and extra low-carbon steels. Metall Trans. 1990;21A:2985–3000. DOI: 10.1007/BF02647219.

[21] Every R, Hatherly M. Oriented nucleation in low-carbon steels. Texture Stress Microstruct. 1974;1:183–194. DOI: 10.1155/TSM.1.183.

[22] Choi S-H, Cho JH. Primary recrystallization modelling for interstitial free steels. Mater Sci Eng A. 2005;405:86–101. DOI: 10.1016/j.msea.2005.05.093.

[23] Rajmohan N, Hayakawa Y, Szpunar JA, et al. Neutron diffraction method for stored energy measurement in interstitial free steel. Acta Mater. 1997;45:2485–2494. DOI: 10.1016/S1359-6454(96)00371-0.

[24] Diehl M, Kertsch L, Traka K, et al. Site-specific quasi *in situ* investigation of primary static recrystallization in a low carbon steel. Mater Sci Eng A. 2019;755:295–306. DOI:10.1016/j.msea.2019.02.032.

[25] Oyarzabal M, Guerenu A, Gutiérrez I. Effect of stored energy and recovery on the overall recrystallization kinetics of a cold rolled low carbon steel. Mater Sci Eng A. 2008;485:200–209. DOI: 10.1016/j.msea.2007.07.077.

[26] Alaneme KK, Okotete EA. Recrystallization mechanisms and microstructure development in emerging metallic materials: A review. J Sci-Adv Mater Dev. 2019;4:19–33. DOI: 10.1016/j.jsamd.2018.12.007.

[27] Seo M-D, Shi C-B, Wang H, et al. Non-isothermal melt crystallization of cuspidine in CaO–SiO2–CaF2 based glasses. J Non-Cryst Solids. 2015;412:58–65. DOI: 10.1016/j.jnoncrysol.2015.01.008.

[28] Umar M, Qayyum F, Farooq MU, et al. Investigating the effect of cementite particles size and distribution on local stress and strain evolution in spheroidized medium carbon steel using crystal plasticity-based

numerical simulations. Steel Res Int. 2021;92:2000407. DOI: 10.1002/srin.202000407.

[29] Qayyum F, Guk S, Prahl U. Studying the damage evolution and the micro-mechanical response of X8CrMnNi16-6-6 TRIP steel matrix and 10% zirconia particle composite using a calibrated physics and crystal-plasticity-based numerical simulation model. Crystals (Basel). 2021;11:759–778. DOI: 10.3390/cryst11070759.

[30] Umar M, Qayyum F, Farooq MU, et al. Qualitative investigation of damage initiation at mesoscale in Spheroidized C45EC steels by using crystal plasticity-based numerical simulations. J Compos Sci. 2021;5:222–240. DOI: 10.3390/jcs5080222.

[31] Saito G, Zhang T, Sakaguchi N, et al. In-situ observation of abnormal grain growth in a low-alloyed carbon steel using SEM-EBSD. Mater. 2021;15:100985. DOI: 10.1016/j.mtla.2020.100985.

[32] Naik SN, Walley SM. The Hall-Petch and inverse Hall-Petch relations and the hardness of nanocrystalline metals. J Mater Sci. 2020;55:2661–2681. DOI: 10.1007/s10853-019-04160-w.

[33] Garcia CI, Deardo AJ. Formation of austenite in 1.5 Pct Mn steels. Metall Trans A. 1981;12:521–530. DOI:doi.org/10.1007/BF02648551.

[34] Riva R, Mapelli C, Venturini R. Effect of coiling temperature on formability and mechanical properties of mild low carbon and HSLA steels processed by thin slab casting and direct rolling. ISIJ Int. 2007;47:1204–1213. DOI: 10.2355/isijinternational.47.1204.

[35] Mishra S, Darmann C. Role and control of texture in deep-drawing steels. Int Met Rev. 1982;27:307–320. DOI: 10.1179/imr.1982.27.1.307.